Chinese Chemical Letters 35 (2024) 108473

Contents lists available at ScienceDirect

Chinese Chemical Letters

journal homepage: www.elsevier.com/locate/cclet

Novel 2D bifunctional layered rare-earth hydroxides@GO catalyst as a functional interlayer for improved liquid-solid conversion of polysulfides in lithium-sulfur batteries

Haodong Wang[a,b,c,e], Xiaoxu Lai[a,c,e], Chi Chen[a,c,e], Pei Shi[d], Houzhao Wan[d], Hao Wang[d], Xingguang Chen[a,b,c,e], Dan Sun[a,c,e,*]

[a] CAS Key Laboratory of Design and Assembly of Functional Nanostructures and Fujian Provincial Key Laboratory of Nanomaterials, Fujian Institute of Research on the Structure of Matter, Chinese Academy of Sciences, Fuzhou 350002, China
[b] College of Chemistry and Materials, Fujian Normal University, Fuzhou 350007, China
[c] Xiamen Institute of Rare Earth Materials, Haixi Institutes, Chinese Academy of Sciences, Xiamen 361021, China
[d] School of Microelectronics, Hubei University, Wuhan 430062, China
[e] Xiamen Key Laboratory of Rare Earth Photoelectric Functional Materials, Xiamen 361021, China

ARTICLE INFO

Article history:
Received 6 March 2023
Revised 4 April 2023
Accepted 18 April 2023
Available online 25 April 2023

Keywords:
Lithium-sulfur batteries
Functional separator
Layered rare-earth hydroxides
Shuttle effect
Adsorption
Catalysis

ABSTRACT

The detrimental "shuttle effect" of lithium polysulfides (LiPSs) together with sluggish multi-order reaction kinetics are the main drawbacks hindering lithium-sulfur (Li-S) batteries from commercial success. Here, we first propose the implementability of layered rare-earth hydroxides (LREHs) in Li-S batteries to optimize electrochemical performance. In this work, a two-dimensional (2D) rare-earth-based composite constructed by the layered gadolinium hydroxy chloride $[Gd_2(OH)_5(H_2O)_n]Cl$ nanoplates (LGdH NPs) and graphene oxide (GO) was designed as a sulfur immobilizer for Li-S batteries. Combining the experimental results and density functional theory (DFT) calculations, it is revealed that the LGdH@GO composite not only provides a strong anchoring of the intermediates during cycling, but also acts as an effective catalyst to accelerate the liquid-solid conversion of polysulfides. The Li-S batteries assembled by LGdH@GO modified separators delivered a superior rate performance with a specific capacity of 605.34 mAh/g at 5 C, as well as excellent cycle stability with a decay rate of 0.087% over 500 cycles at 2 C. This study provided a deep understanding of the mechanism to suppress the "shuttle effect" by the LREHs, and a guide to design effective functional interlayers for high-performance Li-S batteries with excellent electrocatalytic activity.

Lithium-sulfur (Li-S) batteries are promising for the next generation energy storage devices, due to their lightweight design of cells without special thermal management, high security, superior cycling life and environment-friendly traits [1–3]. However, the "shuttle effect" and sluggish reaction kinetics hinder their commercialization and large-scale applications [4]. During cycling, lithium polysulfides (LiPSs) migrate easily between the positive and negative electrode, driven by the concentration gradient and electric field. This results in a dramatic specific capacity loss, low sulfur utilization and corrosion of the lithium metal surface, which not only restrains the formation of a stable solid electrolyte interphase (SEI) but also increases the security risks of the cells [5–7]. On the other hand, sulfur (S_8), Li_2S_2, and Li_2S are poor ionic and electronic conductors [8,9]. Therefore, the effective transport of electrons and ions during the redox reactions are impeded, leading to slow reaction kinetics, large cell polarization, low sulfur utilization and poor rate capability [10–12].

Integrating sulfur with functional materials that feature chemical/physical adsorption and electrocatalytically accelerating the conversion of polysulfides has been validated a root remedy for suppressing its "shuttle effect" and lowing the energy barrier, thus improve cell performance. Recently, various strategies were proposed to settle the above-mentioned issues regarding the material and structural designs [13–16]. Among them, a convenient and effective method to deal with the detrimental "shuttle effect" is to anchor the LiPSs and facilitate a rapid conversion from S_8 to Li_2S [17,18]. Different microstructured (CNT, graphene, 3D carbonaceous gel, *etc.*) and functionalized carbon materials (doping with N, S, B, *etc.*) are known to suppress the LiPSs shuttling [19–22].

* Corresponding author.
E-mail address: xmsundan@fjirsm.ac.cn (D. Sun).

https://doi.org/10.1016/j.cclet.2023.108473
1001-8417/

However, insufficient adsorption sites for LiPSs inhibit the catalytic efficiency. As the conversion between elemental sulfur and LiPSs is a solid-liquid phase transition process, LiPSs can be chemically deposited to form Li_2S, as well as be converted into each other through chemical reactions. Therefore, another strategy to improve the redox reaction kinetics was proposed by the addition of catalytic additives in sulfur hosts [23], electrolytes [24,25], and interlayers [15]. In this regard, metal nano particles (Pt, Ni), single metal-atom doped materials [26,27] and other metal compounds (TiO_2 [28], MoS_2 [18], MXene [29,30], MoN-VN [31]) have shown great potential. Particularly, the metal compounds not only possess high capture abilities to LiPSs, but also reduce the reaction energy barrier of the LiPSs conversion, rendering rapid transport of electrons and efficient utilization of active substances.

Studies correlated with catalytic materials used in Li-S batteries nowadays mainly focus on transition metal elements [32–34], less attentions have been paid on other metals, especially rare earth metal compounds. Compared to the d-block elements, the rare earth (RE) elements possess a unique electronic configuration of $[Xe]4f^{n-1}5d^{0-16}s^2$ ($n = 1$-15) that the unpaired 4f electrons of RE^{3+} do not get involved in the chemical bonding and give rise to special properties, such as luminescence, magnetic moments, catalytic, energy conversion [35,36]. Recently, the significant enhancement of RE oxides, on the chemical adsorption and reaction kinetics of LiPSs was demonstrated, such as La_2O_3 [37], Nd_2O_3 [38], and Y_2O_3 [38]. Among the compounds based on RE elements, layered rare-earth hydroxides (LREHs), an intriguing system of layered host compounds containing lanthanide cations in the host layer, has been explored to offer unique opportunities for functional applications. The general formula of LREHs can be described as: $Ln_8(OH)_{20}A{\cdot}nH_2O$ (Ln = Nd, Sm, Eu, Gd, Tb, Dy, Ho, Er, Tm and Y; A = NO_3, Cl, SO_4) [39,40], the two-dimensional channels with various interlayer spacing of the structure could optimize the ion transport for fast reaction kinetics, providing tunable physical and chemical properties for catalyst design [41,42].

Here, we report a novel LGdH@GO modified polypropylene (PP) separator that exploit a new catalytic combination for Li-S batteries. Specifically, layered gadolinium hydroxy chlorides $[Gd_2(OH)_5(H_2O)_n]Cl$ nanoplates (LGdH NPs) were synthesized under controllable strategies in order to catalyze the LiPSs conversion, while GO acted as a sulfur immobilizer, which endowed better cell performance with enhanced utilization of active material, improved reaction kinetics and rate capability. The LGdH@GO modified separators delivered an excellent discharging capacity of 1039 mAh/g with commercial sulfur particles at the current density of 0.2 C. Moreover, it retained a discharging capacity of 846.8 mAh/g after 100 cycles, and an excellent cycle stability with a decay rate of 0.087% over 500 cycles at 2 C. Benefiting from the first-principal calculations, the chemical evolution of each component can be examined, from which the chemical adsorption and catalytic conversion of polysulfides by LGdH@GO will be verified and studied.

The synthesis process for the LGdH@GO composite is illustrated in Fig. 1a. The LGdH and LGdH@GO composite were synthesized by hydrothermal method using $GdCl_3{\cdot}6H_2O$, NaOH, NaCl, and graphene oxide as raw materials. The detailed preparation process is shown in the Experimental Section in Supporting information. The atomic structure (Fig. 1b) illustrates that the LGdH possesses a zigzag-like layered structure comprising a positively charged $[Gd_8(OH)_{20}(H_2O)_n]^{4+}$ and interlayered Cl ions. The model atoms position of $[Gd_2(OH)_5(H_2O)_n]Cl$ are shown in Table S1 (Supporting information). Gd centered in the main layer, tricapped by Cl and OH groups, the adjacent layers are piled up and stabilized

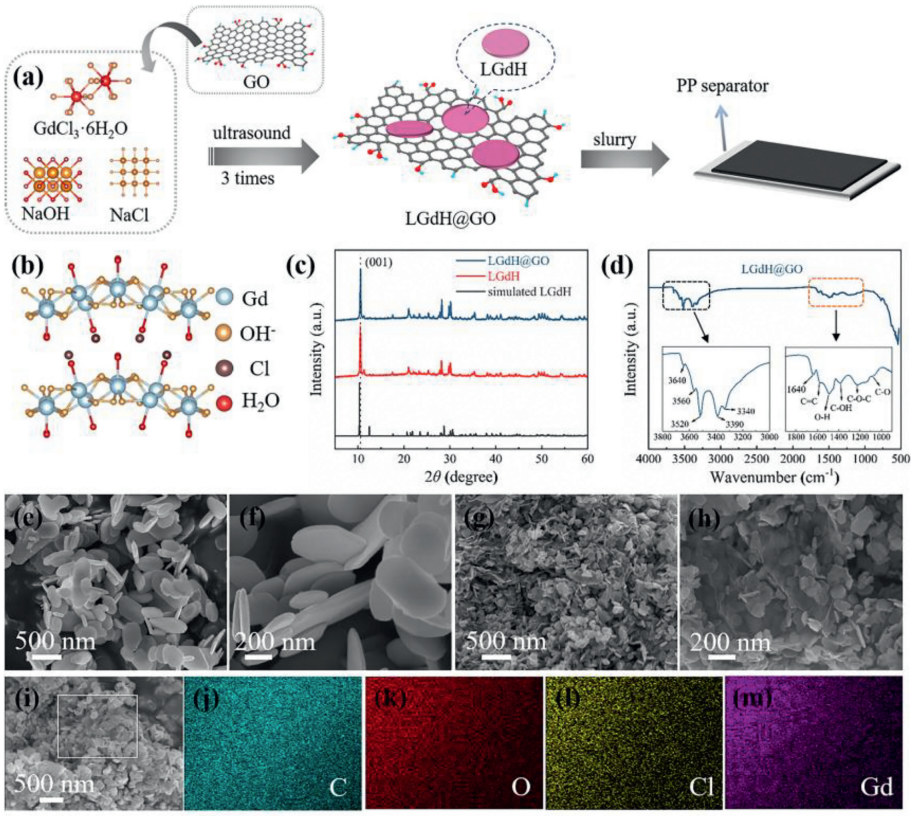

Fig. 1. (a) Schematic illustration for the synthesis of LGdH and LGdH@GO. (b) Crystal structure of $[Gd_2(OH)_5(H_2O)_n]Cl$. Gd, Cl and OH^- species are depicted in blue, orange and brown. (c) XRD patterns of simulated LGdH and synthesized LGdH and LGdH@GO. (d) FTIR spectrum of LGdH@GO. The insets are the FTIR spectra of LGdH@GO at wavenumber from 3000 cm^{-1} to 3800 cm^{-1} (left) and 900 cm^{-1} to 1900 cm^{-1} (right). SEM images of (e, f) LGdH and (g, h) LGdH@GO. (i) SEM image and the corresponding elements mappings of (j) C, (k) O, (l) Cl and (m) Gd.

by crystal water molecules and Cl ions [43]. The X-ray diffraction patterns of prepared samples are displayed in Fig. 1c. Almost all the observed diffraction peaks can be well indexed by the orthorhombic LREHs unit cell with lattice parameters of $a = 12.64$ Å, $b = 7.13$ Å and $c = 8.59$ Å [44], and a (001) diffraction at $2\theta \approx 10.54°$ indicates an interlayer distance of 8.39 Å. Taking the simulated XRD pattens as a reference, the shoulder peak besides the (001) diffraction peak indicates the presence of an unidentified coexisting phase introduced during synthesis [39,45]. Since the low- and high-hydration phase of LGdH is interconvertible at different humidity levels, thermogravimetric analysis (TGA) of LGdH and LGdH@GO (Fig. S1 in Supporting information) was performed to help further evaluate intercalated water molecules ($n = 1.4$) [43,45]. The Fourier transform infrared spectrometer (FT-IR) spectrum of LGdH@GO is shown in Fig. 1d. Based on the structural consideration of LGdH, the two sets of bands around 3600 cm^{-1} (3640, 3560 and 3520 cm^{-1}) and 3350 cm^{-1} (3390 and 3340 cm^{-1}) can be accordingly attributing to the symmetrical and asymmetrical O−H stretching vibrations of intralayer -OH groups and hydrogen-bonded interlayer water molecules, respectively. A band at 1640 cm^{-1} is assigned to the bending mode of water molecules, and the bands below 1000 cm^{-1} are Gd–O vibration modes [40,44,46]. Also, a band in the FT-IR spectrum consisting of fine structures from 1000 cm^{-1} to 1600 cm^{-1} is associated with stretching vibration of C=C, C–O, C–OH groups of GO, indicating the incorporation of GO. The Raman spectrum of LGdH@GO (Fig. S2 in Supporting information) in 1250–1650 cm^{-1} reveals the characteristic D and G band peaks at 1361.5 and 1613.5 cm^{-1}, assigning to disordered non-sp^2 stretching mode and ordered graphitic sp^2 stretching mode of GO, respectively [47].

In order to investigate the microstructure of each sample, scanning electron microscopy (SEM) and transmission electron microscope (TEM) characterizations have been carried out. As shown in Figs. 1e and f, pure LGdH reveals a well-developed plate-like microcrystalline morphology with a size distribution of 500 nm of average diameter and a thickness of about 50 nm, which is consistent with the characteristics of the layered compound. Upon combining LGdH with GO during synthesis, GO flakes can provide the sites for heterogeneous nucleation of LGdH. As a result, LGdH nanoplates are distributed on GO sheets with a reduced particle size of around 100 nm (Figs. 1g and h), which is beneficial for the enhancement of electrical conductivity attributed to the consecutive electronic pathway through the GO sheet. The elemental mapping by energy-dispersive X-ray spectroscopy (EDX) analysis (Figs. 1i-m) further confirm the uniform distribution of LGdH nanoplates on GO sheets. Figs. 2a-c show the TEM images of the LGdH and LGdH@GO, respectively. Pure LGdH exhibits Quasi-hexagonal-platelets morphology, which shares similar morphology with previous reports and suggests a high crystallinity, while nanoplates with reduced size and no obvious features can be observed with LGdH@GO [45]. The SAED pattern taken from an individual platelet of LGdH is clearly demonstrated in Figs. 2d and e [44,45]. In particular, the brighter spots were ascribed to a fundamental cell in a pseudohexagonal symmetry ($af = 3.52$ Å), whereas the arrangement in the reciprocal lattice corresponded to a rectangular supercell ($as = 2\sqrt{3}af = 12.19$ Å; $bs = 2af = 7.04$ Å). Notably, there is slight deviations of the estimated lattice results from simulated parameters.

The specific surface areas (Fig. S3 in Supporting information) of LGdH and LGdH@GO were measured as 15.16 and 54.06 m^2/g, respectively, which indicates the enhancement in the adsorption ability to LiPSs. The chemical compositions of the two samples were also evaluated using X-ray photoelectron spectroscopy (XPS). The peaks at 282.4, 283.3 and 287.2 eV of XPS spectrum of LGdH@GO (Fig. 2f) could be ascribed to C–C, C–O and O–C=O, respectively [48]. The existence of C–O and O–C=O confirmed the successful composite formation of LGdH with GO. The high-resolution XPS spectra in the O 1s region (Fig. 2g) exhibit two peaks at 529.3 and 530.1 eV, which are consistent with O–H and O^{2-}. In the Cl 2p region (Fig. 2h), there were two peaks at 196.3 and 197.7 eV, which are consistent with Cl $2p_{3/2}$ and Cl $2p_{1/2}$. The XPS spectra in the Gd 3d region (Fig. 2i) depicted two satellite peaks at 1197.2 and 1226.8 eV, and two characteristic peaks

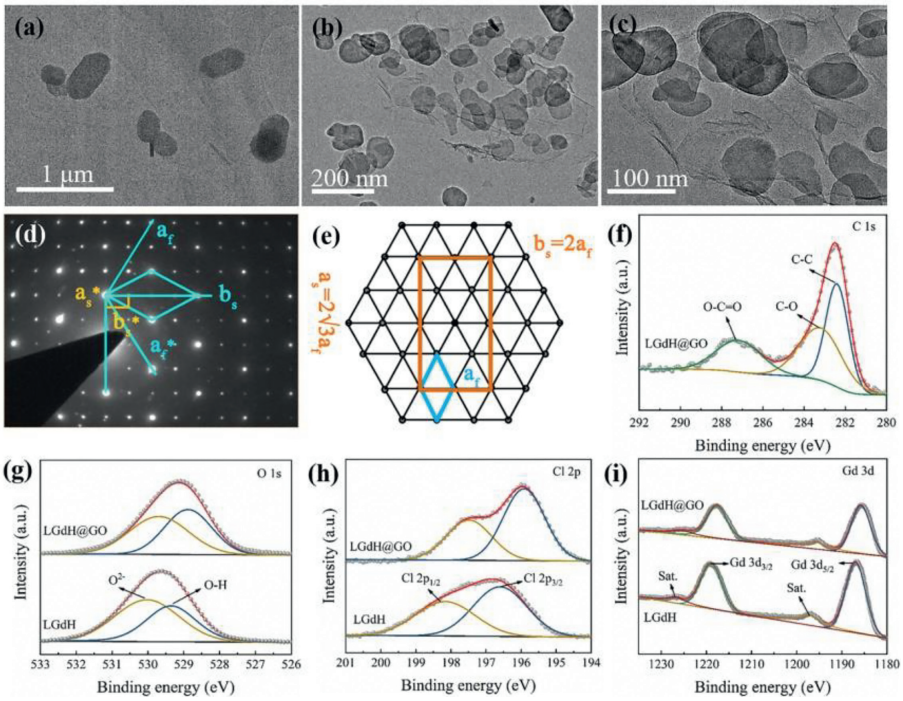

Fig. 2. TEM images of (a) LGdH and (b, c) LGdH@GO. (d) SAED pattern of LGdH. (e) The relationship between the fundamental cell and the rectangular supercell. af: axis of fundamental cell in the real place; as, bs: a and b axes of superlattice cell in the real place, respectively. Labels with asterisks corresponding to reciprocal axes. XPS spectra of (f) C 1s of LGdH@GO. (g) O 1s of LGdH and LGdH@GO. (h) Cl 2p of LGdH and LGdH@GO. (i) Gd 3d of LGdH and LGdH@GO.

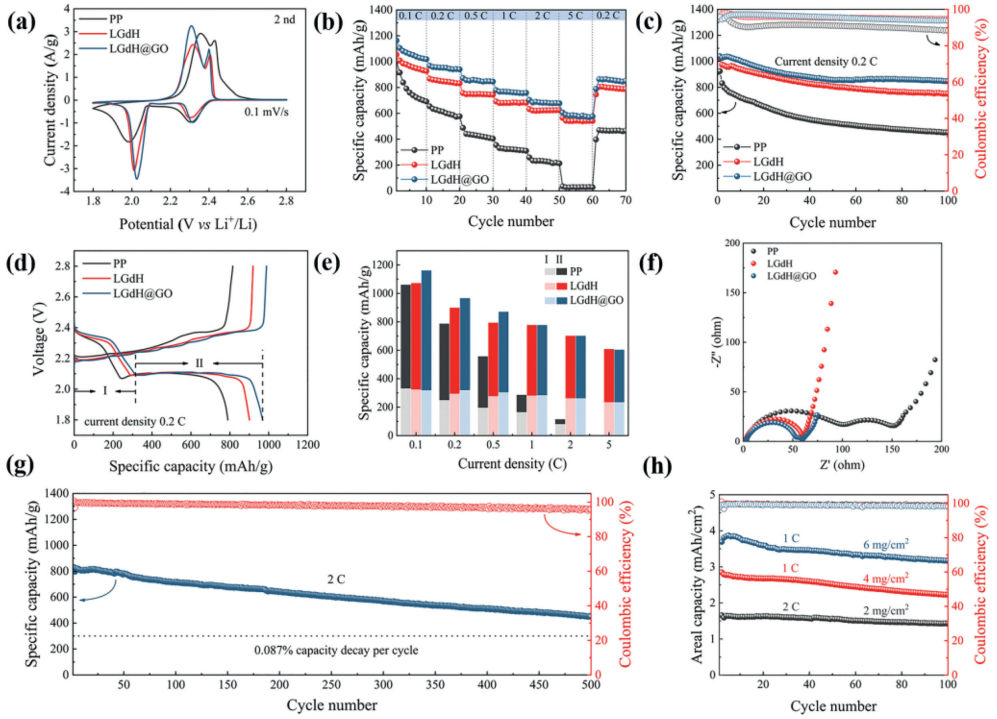

Fig. 3. Electrochemical performances of commercial PP separator, LGdH and LGdH@GO modified separators (sulfur loading of about 1.5 mg/cm^2). (a) CV curves of Li-S batteries with different separators at a scan rate of 0.1 mV/s. (b) Rate performances of Li-S batteries at various current density from 0.1 C to 5 C for different separators. (c) Cycling performances and (d) charge-discharge profiles of Li-S batteries with various separators at 0.2 C. (e) Discharge capacities of Li-S batteries with different separators from the first (denoted as I) and second plateau (denoted as II) at various current densities. (f) EIS spectra of Li-S batteries with various separators from 10 mHz to 100 kHz. (g) Long-term performance of Li-S batteries with LGdH@GO modified separator at a current density of 2 C for 500 cycles. (h) The areal capacity of Li-S batteries with different sulfur loading at the current density of 2 C and 1 C, respectively.

at 1186.9 and 1219.0 eV, which were attributed to Gd $3d_{5/2}$ and Gd $3d_{3/2}$, respectively. Notably, compared with LGdH, the O 1s and Cl 2p region of LGdH@GO shifted toward lower binding energy of around 0.4 eV, while about 1.2–1.4 eV shift toward lower binding energy for Gd 3d region of LGdH@GO, this indicates that there is stronger interaction between GO and Gd atoms.

The electrochemical performances of LGdH and LGdH@GO were investigated by assembling Li-S batteries with LGdH and LGdH@GO modified separators. The cyclic voltammetry (CV) curves of various separators are shown in Fig. 3a at a scan rate of 0.1 mV/s between 1.8 V and 2.8 V. LGdH and LGdH@GO modified separators showed two reduction peaks at about 2.31 and 2.02 V, corresponding to the reduction of elemental sulfur to long-chain LiPSs (Li_2S_x, $4 \leq x \leq 8$) and long-chain to short-chain LiPSs (Li_2S/Li_2S_2), respectively. The oxidation peaks at about 2.31 and 2.40 V could be ascribed to the reversible processes. Additionally, the second reduction peaks of modified separators shifted toward higher potential and became much stronger, which indicates a lower polarization and better sulfur utilization. These CV results clearly imply that the LGdH containing functional interlayer support better electrochemical kinetics for LiPSs conversion. The rate performances of PP, LGdH and LGdH@GO modified separators are shown in Fig. 3b at varying current densities from 0.1 C to 5 C. The LGdH@GO modified separator displayed better specific capacities compared with PP and LGdH separators, with values of 1163.26, 968.32, 872.52, 779.33, 703.77 and 605.34 mAh/g at 0.1, 0.2, 0.5, 1, 2 and 5 C, respectively. This indicates that LGdH@GO composite could effectively hinder the "shuttle effect" of the LiPSs. The galvanostatic discharge/charge (GDC) profiles at various current densities (Fig. S4 in Supporting information) were also used to further confirm the rate performances. As shown in Fig. 3c, PP showed a specific capacity of 924.4 mAh/g initially, but only 48.8% capacity (451.4 mAh/g) was retained after 100 cycles. In contrast, the LGdH and LGdH@GO modified separators demonstrated 73.6% (751.4 mAh/g) and 81.5% (846.3 mAh/g) retention of capacity after 100 cycles. The GDC profiles of various separators (Fig. 3d) at the current density of 0.2 C displayed two typical discharge plateaus corresponding to the conversion of sulfur (S_8) to long-chain LiPSs (I) and long-chain LiPSs to short-chain LiPSs (II), respectively. The specific capacities of all three separators faded with the increasing current density, due to the sluggish reduction kinetics of LiPSs. However, approximately 62% of discharge capacity was retained in the second plateau of LGdH, and LGdH@GO modified separators, even at a high current density of 5 C (Fig. 3e and Table S2 in Supporting information) [49]. The electrochemical impedance spectra (EIS) were also measured to further explore the electrochemical performances of the modified separators. The Nyquist plots of modified separators (Fig. 3f) were composed of a semicircle in the high frequency and a straight line in the low frequency, which were ascribed to charge transfer resistance (R_{CT}) and ion diffusion resistance, respectively [9]. Notably, the PP separator showed much larger R_{CT} with two semicircles in the high frequency because of its poor electronic conductivity. The R_{CT} was the smallest for LGdH@GO modified separator due to the synergistic effect of LGdH nanoplates and graphene oxide. The commercialization of Li-S batteries requires long-term cycling stability and high areal capacity. The long-term cycling stability of LGdH@GO (Fig. 3g) with a sulfur loading of 2 mg/cm^2 was measured at the current density of 2 C. It exhibited an initial specific capacity of 797.4 mAh/g at 2 C after one cycle of activation at 0.1 C. After 500 cycles, it maintained a considerable specific capacity of 449.6 mAh/g, accompanied by a high coulombic efficiency of 96%. The specific capacity retention was calculated as 56.4%, and the corresponding capacity decay rate of 0.087% per cycle, revealing an excellent cycling performance of the LGdH@GO modified separator. Its cycling performances at a current density of 1 C with higher sulfur loadings

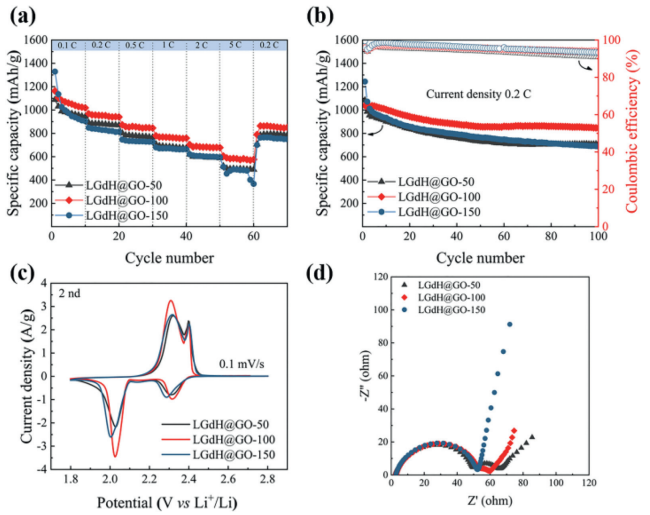

Fig. 4. Electrochemical performances of LGdH@GO-50, LGdH@GO-100 and LGdH@GO-150. (a) Rate performances at various current density of Li-S batteries with various thicknesses. (b) Cycling performances of Li-S batteries with various thicknesses at 0.2 C. (c) CV curves of Li-S batteries with various thicknesses at a scan rate of 0.1 mV/s. (d) EIS spectra of Li-S batteries with various thicknesses.

of 4 and 6 mg/cm^2 was also tested (Fig. 3h). A high initial specific capacity of 2.85 and 3.69 mAh/cm^2 was obtained with one cycle of activation at 0.2 C for samples with 4 and 6 mg/cm^2 of sulfur loadings, respectively, which retained areal capacities of 2.23 and 3.17 mAh/cm^2 after 100 cycles at 1 C, indicating a promising potential in Li-S batteries applications.

Various thicknesses of the LGdH@GO coatings (LGdH@GO-50, 100 and 150) were also prepared for further investigation. The surface morphology and actual thicknesses of LGdH@GO-50, LGdH@GO-100 and LGdH@GO-150 were measured (Figs. S5 and S6, Table S3 in Supporting information) as 19.29, 35.48 and 43.57 μm, respectively. The rate performances of different separators at various current densities are shown in Fig. 4a. LGdH@GO-100 exhibited considerable discharge capacities of 1163.26 mAh/g at 0.1 C and 605.34 mAh/g even at the current density of 5 C. The LGdH@GO-150 showed higher initial capacities of 1329.4 mAh/g at 0.1 C, but with degraded cycling stability. The cycling performances of the samples with various thicknesses were measured at the current density of 0.2 C (Fig. 4b). A superior initial specific capacity of 1039 mAh/g and retention of 846.8 mAh/g after 100 cycles were exhibited by the LGdH@GO-100. In contrast, despite exhibiting the highest initial discharge capacity of 1243.8 mAh/g, the cycling performance of the LGdH@GO-150 retained only 688.4 mAh/g after 100 cycles. The CV curves of interlayers of different thicknesses (Fig. 4c) were measured at a scan rate of 0.1 mV/s. The LGdH@GO-100 delivered stronger redox peaks, corresponding to better utilization of elemental sulfur and a smaller polarization. Fig. 4d shows the EIS spectra of various thicknesses of LGdH@GO modified separators. Notably, LGdH@GO-50 and LGdH@GO-100 exhibited two semicircles in the high frequency, whereas LGdH@GO-150 showed only one semicircle. This can be ascribed to better electronic conductivity for the thicker LGdH@GO coatings. In particular, the optimization of thickness plays a significant role in improving the electrochemical performances in terms of catalytic activity. Consequently, a much thicker LGdH@GO would limit the ion transport, resulting in a worse electrochemical performance.

The adsorption abilities of LGdH and LGdH@GO were assessed by the static polysulfide adsorption test [50]. The interaction between the two samples and LiPSs was verified by a visual distinction using the Li_2S_9 solution. Briefly, a certain amount of LGdH and LGdH@GO powders were separately added into 3 mL 2 mmol/L Li_2S_9 solution. The pronounced adsorption ability to LiPSs of GO has been well verified previously as a result of the abundant functional groups on the surface. As shown in Fig. S7 (Supporting information), solution with 20 mg LGdH@GO turned colorless after 24 h of static adsorption, while for 20 mg LGdH, the color change was not obvious indicating the weaker LiPSs adsorption of LGdH. When increasing the amount of LGdH to 100 mg, the faded solution was mainly due to the raising particle surface area. Quantitative analysis of the adsorption of the LiPSs was provided by ultraviolet (UV)-visible spectroscopic measurements. The observed peak intensity of LGdH@GO was much lower compared with LGdH, which indicated a better polysulfide adsorption ability of LGdH@GO (Fig. 5a). A simple potential discharge experiment corresponding to the nucleation of Li_2S was measured (Figs. 5b and c) to further investigate the ability of LGdH and LGdH@GO in accelerating the liquid-solid conversion progress. A similar growth time of about 3 min was found for both LGdH and LGdH@GO, indicating that LGdH takes main responsibility for the rapid kinetics of Li_2S precipitation. It is worth mentioning that, the capacity of precipitated Li_2S for LGdH@GO (291.67 mAh/g_s) was much higher than LGdH (188.45 mAh/g_s), and it delivered a higher current intensity, which indicates better Li_2S nucleation and more precipitation on LGdH@GO surface [49,51]. A pivotal parameter to reflect the conversion kinetics of lithium polysulfides is the diffusion coefficient of Li ions. The diffusion coefficient of Li ions for the LGdH@GO separator was evaluated from the CV curves (Fig. 5d) under varying scanning rates from 0.1 mV/s to 0.6 mV/s with a voltage range between 1.8 V to 2.8 V (*vs.* Li^+/Li). Corresponding CV curves for PP and LGdH separators are shown in Figs. S8a and b (Supporting information). In addition, a linear correlation with the square root of the scan rates was found for the reduction peaks (peak I and peak II) and oxidation peak current (peak IV) of various separators, which was estimated based on Randles-Sevcik Eq. 1.

$$I_p = 2.69 \times 10^5 n^{1.5} A D_{Li}^{0.5} C_{Li} \nu^{0.5} \quad (1)$$

where I_p, n, A, D_{Li^+}, C_{Li^+}, and ν represent the peak current, electron charge number ($n=2$), electrode area, diffusion coefficient of Li ions, the concentration of Li ions, and the scan rate, respectively [52,53]. Figs. 5e-g show the relationship between I_p and $\nu^{0.5}$, and the slopes of the curves were positively correlated to D_{Li^+}. The slopes of the modified separator were much higher than the PP separator in each redox peak. Additionally, the specific values of various separators at redox peaks are shown in Table 1. The LGdH@GO modified separator showed the highest diffusion coefficient of Li ions, which demonstrates a faster Li ion diffusivity and better LiPSs conversion kinetics compared to the commercial PP separators.

Table 1
Diffusion coefficients of Li ions for various separators.

Separators	PP	LGdH	LGdH@GO
Peak I (cm^2/s)	6.59×10^{-15}	2.96×10^{-14}	4.89×10^{-14}
Peak II (cm^2/s)	2.15×10^{-14}	1.34×10^{-13}	2.16×10^{-13}
Peak IV (cm^2/s)	1.38×10^{-14}	1.89×10^{-13}	3.11×10^{-13}

The chemical interaction between the LiPSs and LGdH was further investigated using the DFT simulations. The configurations of Li_2S, Li_2S_2, Li_2S_4, Li_2S_6, Li_2S_8 and S_8 on the LGdH (001) surface were chosen as the computational models [54]. Interestingly, S_8, Li_2S_8, and Li_2S_6 decomposed quickly when adsorbed on the LGdH surface as shown in Fig. 6a, indicating a strong catalytic ability on LiPSs conversion from the long-chain LiPSs into short-chain LiPSs. The relaxed configurations of Li_2S, Li_2S_2 and Li_2S_4 on LGdH (001) surface were shown in Fig. 6a and the corresponding binding energies were calculated to be −2.97, −5.82 and −5.99 eV, respectively, indicating a strong chemical adsorption [51]. The calculation

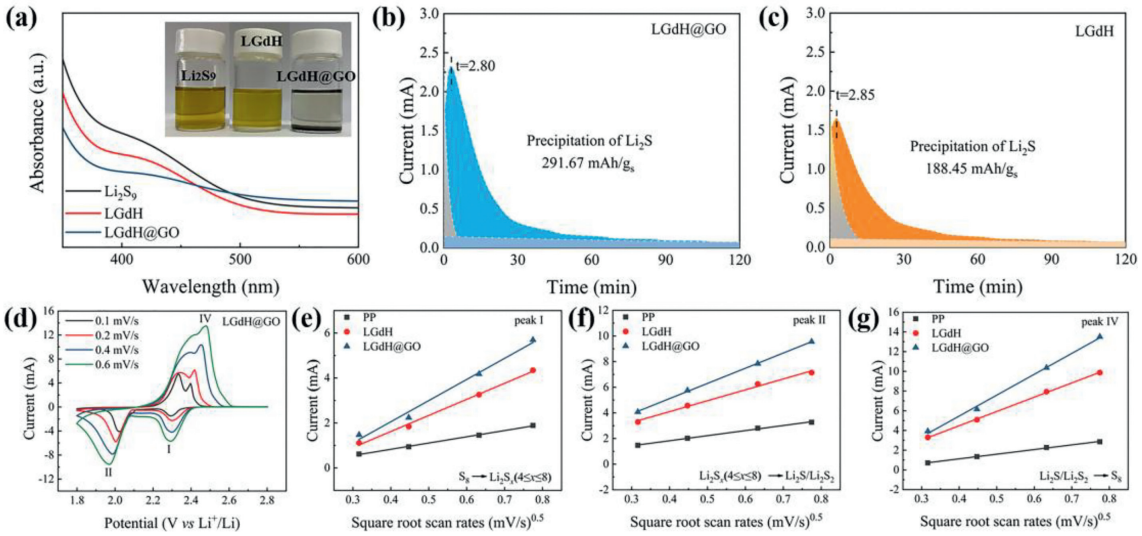

Fig. 5. (a) Ultraviolet (UV)-visible spectra of Li_2S_9 solution mixed with various samples. The inset is a digital image of polysulfides (Li_2S_9) adsorption test after 24 h. Potentiostatic discharge profiles of Li_2S_8 solution on (b) LGdH@GO and (c) LGdH at 2.05 V. (d) CV curves of Li-S battery with LGdH@GO modified separator at various scan rates. Plots of peak current for (e) the first cathodic reduction process, (f) second cathodic reduction process, and (g) anodic oxidation process with the square root of the scan rate ($v^{1/2}$) of the Li-S batteries with PP separator, LGdH and LGdH@GO modified separators.

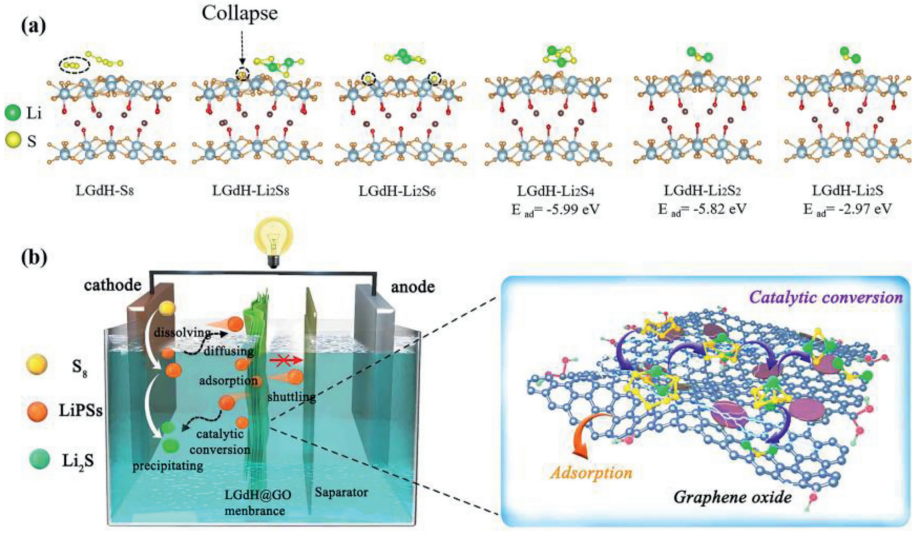

Fig. 6. (a) Relaxed configurations of S_8, Li_2S_8, Li_2S_6, Li_2S_4, Li_2S_2 and Li_2S on LGdH surface. (b) Schematic illustration of the catalytic conversion mechanism of LiPSs on LGdH@GO surface.

results were in good agreement with the electrochemical measurements and the LiPSs adsorption experiment, which confirmed the ability of LGdH to accelerate the chemical reaction kinetics during the discharge/charge progress, leading to better electrochemical performances. The catalytic conversion mechanism of LiPSs to Li_2S for the presence of LGdH@GO modified separators is illustrated in Fig. 6b. While the pristine PP separator was only considered as an inhibitor for LiPSs, the LGdH@GO interlayer not only provided a strong chemical adsorption but also accelerate the catalytic redox conversion of LiPSs.

In summary, LGdH@GO composite was prepared using a simple hydrothermal method for the modification of the PP separators in Li-S batteries. The remarkable electrochemical performances of the LGdH@GO modified separator were confirmed by combining the experimental investigations and DFT calculations. The liquid-solid conversion of LiPSs was accelerated by the LGdH nanoplates due to their efficient electrocatalytic activity and strong chemical affinity to LiPSs. Moreover, benefiting from the fast transport channels for electrons/ions and abundant functional groups in company with the incorporation of GO, LGdH@GO composite helps further facilitates the reaction kinetics and enhances the adsorption ability toward LiPSs. Therefore, the LGdH@GO modified separator displayed excellent electrochemical performance, with values of 1163.26, 968.32, 872.52, 779.33, 703.77 and 605.34 mAh/g at the current densities of 0.1, 0.2, 0.5, 1, 2 and 5 C, respectively. Also, the LGdH@GO contributed to excellent cycling stability with a decay rate of only 0.087% over 500 cycles at a current density of 2 C. The current study demonstrated a novel strategy for the first application of LREHs in high-performance Li-S batteries due to their excellent electrocatalytic performance, the catalytic abilities of LGdH have also been systematically investigated, aiming to lay the foundation for the future application of LREHs in Li-S batteries.

Declaration of competing interest

The authors declare that they have no known competing financial interests or personal relationships that could have appeared to influence the work reported in this paper.

Acknowledgment

This work was supported by National Science Foundation for Youths of China (Nos. 22209184 and 22109163).

Supplementary materials

Supplementary material associated with this article can be found, in the online version, at 10.1016/j.cclet.2023.108473.

References

[1] Y. Ansari, S. Zhang, B. Wen, F. Fan, Y.M. Chiang, Adv. Energy Mater. 9 (2019) 1802213.
[2] F. Pei, L. Lin, A. Fu, et al., Joule 2 (2018) 323–336.
[3] X. Liu, H.J. Peng, B.Q. Li, et al., Angew. Chem. Int. Ed. 134 (2022) e202214037.
[4] C.L. Song, G.H. Li, Y. Yang, et al., Chem. Eng. J. 381 (2020) 122701.
[5] G. Jiang, N. Zheng, X. Chen, et al., Chem. Eng. J. 373 (2019) 1309–1318.
[6] H. Zhang, W. Zhao, M. Zou, et al., Adv. Energy Mater. 8 (2018) 1800013.
[7] X.Z. Fan, M. Liu, R. Zhang, et al., Chin. Chem. Lett. 33 (2022) 4421–4427.
[8] X. Li, Y. Zhang, S. Wang, et al., Nano Lett. 20 (2020) 6922–6929.
[9] M. Kim, J. Lee, Y. Jeon, Y. Piao, Nanoscale 11 (2019) 13758–13766.
[10] Y. Li, W. Wang, X. Liu, et al., Energy Stor. Mater. 23 (2019) 261–268.
[11] Y.Q. Peng, M. Zhao, Z.X. Chen, et al., Nano Res. (2022) 1–7.
[12] M. Zhao, Y.Q. Peng, B.Q. Li, X.Q. Zhang, J.Q. Huang, J. Energy Chem. 56 (2021) 203–208.
[13] L. Ma, R. Chen, G. Zhu, et al., ACS Nano 11 (2017) 7274–7283.
[14] N. Zhang, Y. Yang, X. Feng, et al., J. Mater. Chem. A 7 (2019) 21128–21139.
[15] G.K. Gao, Y.R. Wang, S.B. Wang, et al., Angew. Chem. Int. Ed. 133 (2021) 10235–10242.
[16] S. Guo, Y. Xiao, J. Wang, et al., Nano Res. 14 (2021) 4556–4562.
[17] Y. Wang, Z. Deng, J. Huang, et al., Energy Stor. Mater. 36 (2021) 466–477.
[18] R. Wang, C. Luo, T. Wang, et al., Adv. Mater. 32 (2020) 2000315.
[19] J. Xu, W. Zhang, Y. Chen, et al., J. Mater. Chem. A 6 (2018) 2797–2807.
[20] J. Park, B.C. Yu, J.S. Park, et al., Adv. Energy Mater. 7 (2017) 1602567.
[21] L. Wang, Z. Dong, D. Wang, F. Zhang, J. Jin, Nano Lett. 13 (2013) 6244–6250.
[22] Y. Hwa, H.K. Seo, J.M. Yuk, E.J. Cairns, Nano Lett. 17 (2017) 7086–7094.
[23] B. Liu, R. Bo, M. Taheri, et al., Nano Lett. 19 (2019) 4391–4399.
[24] C. Luo, E. Hu, K.J. Gaskell, et al., Proc. Natl. Acad. Sci. U. S. A. 117 (2020) 14712–14720.
[25] L. Kong, L. Yin, F. Xu, et al., J. Energy Chem. 55 (2021) 80–91.
[26] L. Zhang, D. Liu, Z. Muhammad, et al., Adv. Mater. 31 (2019) 1903955.
[27] Z. Du, X. Chen, W. Hu, et al., J. Am. Chem. Soc. 141 (2019) 3977–3985.
[28] K. Gao, R. Xu, Y. Chen, et al., Chin. Chem. Lett. 34 (2023) 107229.
[29] Q. Gu, M. Lu, J. Chen, Y. Qi, Particuology 57 (2021) 139–145.
[30] D. Guo, F. Ming, H. Su, et al., Nano Energy 61 (2019) 478–485.
[31] C. Shang, G. Li, B. Wei, et al., Adv. Energy Mater. 11 (2021) 2003020.
[32] Q. Liu, Y. Wu, D. Li, et al., Adv. Mater. 32 (2022) 2209233.
[33] Y. Mo, L. Liao, D. Li, et al., Chin. Chem. Lett. 34 (2023) 107130.
[34] Z. Ye, Y. Jiang, L. Li, F. Wu, R. Chen, Adv. Mater. 32 (2020) 2002168.
[35] P. Chen, W. Han, M. Zhao, et al., Adv. Funct. Mater. 31 (2021) 2008790.
[36] J. Xu, X. Chen, Y. Xu, Y. Du, C. Yan, Adv. Mater. 32 (2020) 1806461.
[37] D. Liu, C. Zhang, G. Zhou, et al., Adv. Sci. 5 (2018) 1700270.
[38] P. Zeng, M. Chen, J. Luo, et al., ACS Appl. Mater. Interfaces 11 (2019) 42104–42113.
[39] F. Geng, Y. Matsushita, R. Ma, et al., J. Am. Chem. Soc. 130 (2008) 16344–16350.
[40] J. Liang, R. Ma, T. Sasaki, Dalton Trans. 43 (2014) 10355-10364.
[41] X. Wang, X. Li, X. Du, et al., Inorg. Chem. 29 (2017) 1286–1293.
[42] F. Lan, H. Zhang, J. Fan, et al., ACS Appl. Mater. Interfaces 13 (2021) 2734–2744.
[43] S.S. Lee, B.I. Lee, S.J. Kim, S.H. Byeon, J.K. Kang, Inorg. Chem. 51 (2012) 10222–10232.
[44] F. Geng, H. Xin, Y. Matsushita, et al., Chem. Eur. J. 14 (2008) 9255–9260.
[45] B.I. Lee, K.S. Lee, J.H. Lee, I.S. Lee, S.H. Byeon, Dalton Trans. (2009) 2490–2495.
[46] Y. Xu, A. Goyanes, Y. Wang, et al., Dalton Trans. 47 (2018) 3166–3177.
[47] F. Xu, C. Dong, B. Jin, et al., J. Electroanal. Chem. 876 (2020) 114545.
[48] J. Li, C. Chen, Y. Chen, et al., Adv. Energy Mater. 9 (2019) 1901935.
[49] H. Li, C. Chen, Y. Yan, et al., Adv. Mater. 33 (2021) 2105067.
[50] H.J. Peng, Z.W. Zhang, J.Q. Huang, et al., Adv. Mater. 28 (2016) 9551–9558.
[51] T. Sun, X. Zhao, B. Li, et al., Adv. Funct. Mater. 31 (2021) 2101285.
[52] W. Li, J. Qian, T. Zhao, et al., Adv. Sci. 6 (2019) 1802362.
[53] G. Zhou, H. Tian, Y. Jin, et al., Proc. Natl. Acad. Sci. U. S. A. 114 (2017) 840–845.
[54] L. Li, L. Chen, S. Mukherjee, et al., Adv. Mater. 29 (2017) 1602734.